Reaction Chemistry & Engineering

Non-Premixed Reactive Volatilization Reactor for Catalytic Partial Oxidation of Low Volatility Fuels at a Short Contact Time

Journal:	*Reaction Chemistry & Engineering*
Manuscript ID	RE-ART-12-2020-000460.R1
Article Type:	Paper
Date Submitted by the Author:	31-Jan-2021
Complete List of Authors:	Lin, Ying; University of Minnesota Twin Cities, Mechanical Engineering Li, Xuesong; University of Minnesota Twin Cities, Department of Mechanical Engineering; Shanghai Jiao Tong University, Department of Mechanical Engineering Twigg, Martyn; TST Ltd Northrop, William; University of Minnesota Twin Cities, Department of Mechanical Engineering

Non-Premixed Reactive Volatilization Reactor for Catalytic Partial Oxidation of Low Volatility Fuels at a Short Contact Time

Ying Lin[a], Xuesong Li[a†], Martyn V. Twigg[b] and William F. Northrop[a*]

[a]Department of Mechanical Engineering, University of Minnesota – Twin Cities, Minneapolis, MN 55455, USA.
[b]Twigg Scientific & Technical Ltd, Caxton, Cambridge CB23 3PQ, UK
[†]Current affiliation: Shanghai Jiao Tong University, School of Mechanical Engineering, 800 Dongchuan Road, Shanghai 200240, China

*Correspondence should be sent to: wnorthro@umn.edu, (612) 625 6854

Electric Supplementary Information (ESI) available

ABSTRACT

This work presents a novel non-premixed opposed-flow reactive volatilization reactor that simultaneously vaporizes and partially oxidizes low volatility liquid hydrocarbons at a short contact time (<12 ms). In the reactor, a catalyst-coated metal mesh is placed interstitially between an air duct and a liquid pool. Low-volatility fuels are evaporated from radiative and convective heating and combine at local stoichiometry determined by the axial location of the mesh. Experiments were conducted with n-dodecane at different local molar carbon-to-oxygen ratio (*C/O*) and inlet airflow. Platinum and rhodium coated mesh substrates were the active materials to perform partial oxidation. A 1-D opposed-flow similarity model based on the canonical opposed-flow combustion solution was created to simulate the axial temperature and species concentration along the reactor centerline. Results show that the reactor vaporized and converted n-dodecane to reformed products at a global molar carbon-to-oxygen ratio $(C/O)_g$ up to 3.46. However, the local mixture, with $(C/O)_{mesh}$ ranged from 0.2 to 3.94 for platinum and 0.31 to 4.97 for rhodium. It was found that local stoichiometry at the mesh surface plays a more important role than the

global since no gas-phase reactions occurred outside the mesh region. Overall, our work demonstrates that non-premixed catalytic reactive volatilization is a promising technique to investigate fundamental concepts in hydrocarbon reforming and can offer insights for designing practical short-contact time reactors that can have high conversion and selectivity but low surface carbon deposition tendency at high *C/O*.

INTRODUCTION

Background

Catalytic partial oxidation (CPOx) hydrocarbon reforming is an established process that produces hydrogen and carbon oxide-containing syngas, and is used to manufacture a wide range of valuable industrial products[1-3]. The process can also be scaled down to produce hydrogen for compact fuel cell systems[4-6], and to improve thermal efficiency and pollutant emissions of internal combustion engines[7-9]. Small-scale reforming systems sometimes require the use of market-available liquid hydrocarbon fuels like diesel, gasoline, and their derivatives [6, 10]. Although CPOx is commonly used industrially, the process is still not completely understood, especially for heavier hydrocarbons than those found in natural gas. For example, detailed reaction mechanisms of CPOx over common catalysts containing Ni and Pt have been published for natural gas [11-13], but are less available for reforming of heavier feedstocks [14, 15].

Catalyst deactivation by carbon deposition has long been a constraint for CPOx reactors [15, 16] due to a lack of steam availability and high reaction temperatures with fuel-rich reactant mixtures. Higher molecular weight hydrocarbons found in conventional liquid fuels pyrolyze at lower temperatures have a higher propensity for carbon deposition in CPOx reactors. For this reason,

operation is usually limited to a low global molar carbon-to-oxygen ratio (C/O_g<2), thus limiting the desired product type and concentration. When available, steam is introduced as a reactant to prohibit carbon formation and enable additional steam reforming to increase hydrogen yields. However, in small-scale CPOx reactors and some industrial plants, process steam is not readily available or is too expensive.

Reforming liquid feedstocks with CPOx and pyrolysis in traditional premixed plug flow reactors has been studied by others[14, 17, 18]. Disadvantages of premixed CPOx reactors include undesirable gas-phase reactions that occur upstream of the catalyst, carbon deposition, catalyst deactivation due to hot spots, self-ignition due to high fuel reactivity, and insufficient steam availability to suppress carbon deposition. A high preheat temperature is known to induce pre-ignition of the mixture before the catalyst[19]. Temperature control more broadly is challenging in CPOx reactors at near-adiabatic conditions. A higher reaction temperature in local areas of the bed can cause hot spots and catalyst deactivation through sintering[17].

The requirement to vaporize liquid fuels prior to CPOx reactors presents a complication in their use since many heavy hydrocarbons thermally decompose at temperatures near or below their boiling point [20-22]. A desire to vaporize and reform liquid feedstocks while limiting carbon deposition has motivated novel short-contact time reactor concepts. For example, Schmidt et al. studied short contact time (5-25 ms) CPOx flash volatilization reactors, where rapid oxidation kinetically limited soot formation on the catalyst surface[14, 20]. Even though the conversion rate was high for these reactors, they were still limited to a *C/O* ratio below 3.0, and a relatively narrow temperature range to avoid coke formation and homogeneous gas-phase oxidation reactions. [14, 22]

Non-premixed reactors are commonly used in experimental flame studies[23]. In particular, opposed-flow stagnation reactors and their derivatives can be seen as analogs to non-premixed catalytic reactors. When applied to catalytic reactions, non-premixed reactors show the advantage of avoiding high-temperature rich regions that cause carbon formation by separating fuel vapor and oxidizer using a reaction zone. Some previously developed non-premixed CPOx reactors have used radiative heat transfer from the catalyst surface to evaporate liquid hydrocarbons from a surface adjacent to the catalyst[24]. Others have utilized a catalytic fluidized-bed based on copper as the active material [25]. They demonstrated that catalyst thermal deactivation or catalyst loss by attrition did not occur over the experimental period. One issue present in the analysis of non-premixed reactors is predicting local stoichiometry since direct sampling can influence the mixture at a given location. Such prediction must rely on numerical modeling to interpret experimental results [26].

Non-Premixed Short Contact Time Reactor

In this work, a novel non-premixed reactive volatilization reactor was developed, inspired by previous non-premixed reforming reactors[24] and canonical opposed-flow flame reactors used in combustion research [23, 27, 28] as illustrated in Figure 1(a). Opposed-flow reactors generally introduce unmixed reactants from opposite sides of the reaction chamber. In the combustion reactor case, a laminar flame is established at the axial location with ideal air and fuel stoichiometry, sometimes at a different location than the stagnation plane. Fuel is evaporated from the pool driven by heat generated by the flame. Opposed-flow flame reactors are used to study gas-phase chemistry in a controlled and well- understood geometry.

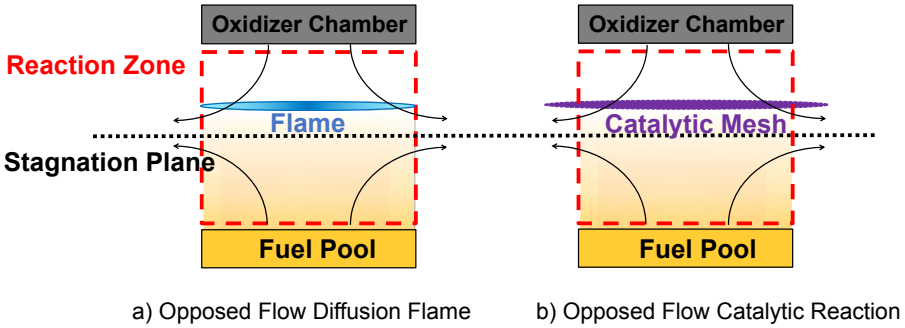

Figure 1. Schematics of opposed flame reactor and opposed-flow catalytic reformer.

In the case of the opposed-flow catalytic reactor, as shown in Figure 1(b), a circular catalytic mesh is interstitially placed between the liquid fuel pool and the air plenum. Low activation energy at the catalytic surface allows the mesh to take the place of the flame at lower temperatures than are found in flame reactors. The heat from the reaction on the metallic mesh drives evaporation of the fuel allowing vapor to diffuse to the catalyst surface. Local carbon-to-oxygen ratio of the oxidation reaction (C/O_{mesh}) at the catalyst can be varied by changing the axial position of the mesh or by varying the flow rate of air. In this work, C/O_{mesh} is defined as the carbon-to-oxygen ratio on the catalyst surface, where fuel and air concentrations are dependent on both bulk flow and species diffusion.

One unique advantage of the opposed-flow reactor arrangement is that the reaction zone is not contained in a closed duct, which provides access for both traditional diagnostics like probe sampling and for optical diagnostics to measure species temperature and concentration. Optical methods like tracer planer laser-induced fluorescence (PLIF) are commonly used in combustion research to measure *in-situ* temperature or species concentration within flames and can be applied

to catalytic reactions in the developed reactor design [29]. Using more comprehensive diagnostics allows better understanding of gas and surface phase chemistry and transport mechanisms.

An advantage of using opposed-flow reactors in combustion research, and the primary method by which chemical kinetics and transport are derived from experiments, is that they can be accurately modeled using a simple quasi-one-dimensional numerical model[23, 30]. The opposed-flow catalytic reactor configuration 2-D problem can also be modeled using a similar spatially one-dimensional simplification. This model can be used to explain observations and determine the key parameters for experiments [12, 13, 31].

The objective of this research was to experimentally characterize an opposed-flow catalytic reactor concept that simultaneously vaporizes low volatility liquid fuels. As a principal study, this prototype reactor successfully demonstrated how liquid fuel reforming could be achieved using the opposed flow configuration. The reactor was fueled by dodecane with platinum and rhodium active catalyst materials wash coated onto metal mesh substrates. Gas-phase temperature and species composition are reported from the reaction zone to evaluate catalytic activity while the open accessibility of the reactor allowed optical measurements of the flow using planar laser-induced fluorescence.

METHODOLOGY

Bench-Scale Reactive Volatilization Reactor

A bench-scale opposed-flow reactive volatilization reactor (illustrated in Fig. 2) was designed to study non-premixed reforming and related processes. The reactor incorporates a circular duct for gaseous

reactants in the top-most chamber and an open reservoir in the mid-level chamber containing liquid hydrocarbon fuel (n-dodecane (n-$C_{12}H_{26}$) in this work). A circular catalytic mesh was placed between the top and mid-level chambers at a pre-set distance above the fuel pool as shown in Fig. 2(a). The gaseous oxidizer (air) was preheated to ~550 °C using an external electric inline heater before entering the inner chambers. Ten 200-mesh (74 μm hole size) stainless steel meshes were stacked in the inner chamber to settle the flow and a section of ceramic honeycomb (1 inch thickness, 1 mm^2 mesh size) was used as a flow straightener prior to the reaction zone as recommended in [32]. A hot wire anemometer sensor was used to measure velocity variation as a function of location in the reacting zone. These measurements found that the spatial velocity variation was within 4%, except for the area very close to the wall over the range of tested experimental conditions. A nitrogen purge was applied outside the reaction zone to prevent diffusion of fuel into the laboratory environment and diffusion of excess oxidizer into the reaction zone.

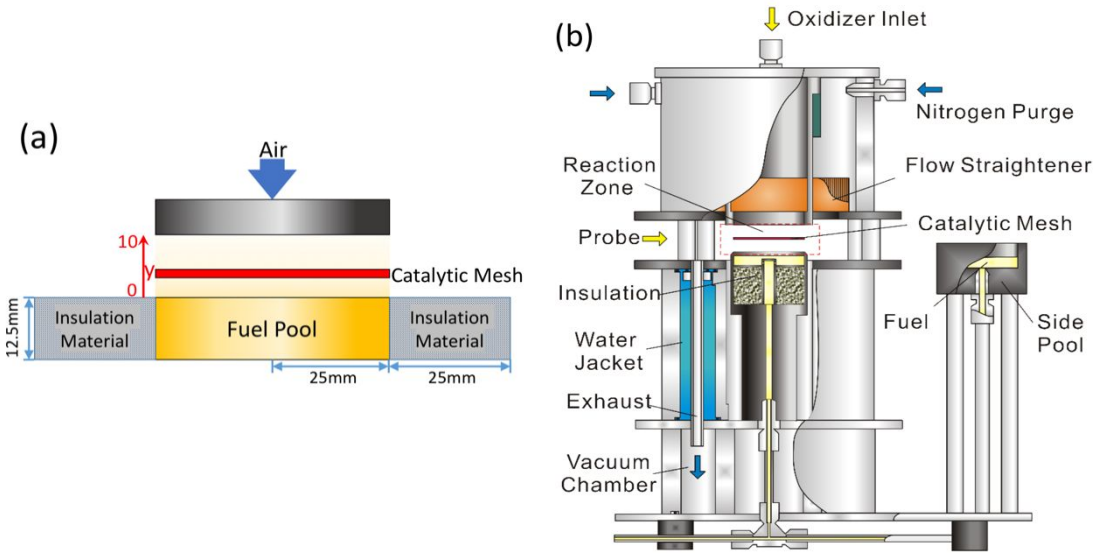

Figure 2. Diagram of the experimental setup: (a) reaction zone (b) reactor.

A 1.5 mm thick ring support was used to securely hold the catalytic mesh in place. The catalytic mesh is hung on the support ring with wires. The support ring is outside of the reaction zone and does not disturb the flow through the mesh in any way. Flow visualization experiment shows the catalytic mesh has minimum effect to the flow. The height (axial position) of the ring support/mesh was controlled by a linear translation stage with 10 micrometer resolution. Ceramic wool was used as the insulation material in the liquid fuel pool to reduce heat loss due to heat conduction to the reactor body (~3% estimated conduction loss). A heat exchanger surrounded the fuel pool to evacuate and cool the exhaust from the reaction zone. This prevented auto-ignition of unburned gases and reformed products. A side pool was connected to the central pool for easy fuel level determination; and a syringe pump-controlled the fuel flow rate. The distance between the air duct and fuel pool was adjustable by replacing spacers and was set to 10 mm throughout the experiments for consistency with previous work [32].

Wire meshes (50 mm diameter) made from 0.3 mm thick Kanthal-D (FeCralloy) wire (18 mesh/inch) with an open area of 61.6% were used as the catalyst substrate. To prepare the catalyst, the meshes were degreased via three treatments with 70 °C aqueous nonionic detergent for 30 minutes, rinsed four times with 30 °C deionized water before rinsing with pure acetone and then air-dried. The degreased meshes were heated in ambient air at 500 °C for 3 hours in order to develop a surface oxide layer to facilitate adhesion of washcoat prepared by ball milling a thermally stable silica/alumina (20% dry solids) in deionized water overnight. Each mesh was immersed in washcoat before excess was shaken off and the meshes were dried at 150 °C before heating at 550 °C for 5 hours. The process was repeated twice more to produce a uniform, strongly adhering coating (25 to

30 μm thick from microscopic measurements). Coated meshes were impregnated with a $Pt(NH_3)_4(NO_3)_2$ or $Rh(NO_3)_3$ washcoat solution to generate a precious metal loading on the washcoat at a concentration close to 1.0 % by mass. The resulting approximate active metal loading per volume of substrate was 1.65 mg/m^3.

To measure the spatial temperature distribution in the reaction zone, a K-type thermocouple with a diameter of 400 μm was used. It was expected that since the radical concentrations of the reactants away from the catalytic mesh were sufficiently low, catalytic reactions on the thermocouple could be neglected [33]. Errors due to heat transfer to the thermocouple were also ignored based on a heat-balance calculation and the relatively low operating temperature of the reactor [34, 35]. Limited by the space and error that might be induced due to direct contact, the temperature of the catalytic mesh surface was measured with a non-intrusive infrared thermometer. The temperature readings using this thermometer were verified by comparing to a very thin thermocouple (K-type, D=0.025 mm) temporarily attached to the mesh. To sample the reaction products and conduct speciation analysis, an uncooled quartz microprobe (2.0 mm in diameter) with a small orifice inlet was used [36]. The orifice size (initially 50 μm) was slightly adjusted by grounding for an appropriate flow rate. The quartz probe (or the thermocouple) was fixed on a linear translation stages (0.02 mm adjustment resolution) with both axial and radial position control.

A Raman laser gas analyzer (RLGA) system (Atmosphere Recovery Inc., Model RLGA-1800L-BF) was used to evaluate light reaction products, such as hydrogen and carbon monoxide generated by catalytic reforming reactions. In addition to the total hydrocarbon concentration speciation by RLGA, a micro gas chromatography (micro-GC) system (Agilent Micro GC 490) with two columns

(PPU BF and 5CB) was used to quantify detailed light hydrocarbon species. A customized gas sampling system was implemented to sample reaction products and store the sample in a heated stainless reservoir. The collected gas sample was then injected into the RLGA and micro-GC. The sampling flow rate was set to be 200 mL/min for the RLGA and 50 mL per run for the micro-GC. A chiller consisting of multiple ice-water-cooled bubblers was implemented to remove any heavy hydrocarbon in the sample gas, including unreacted n-dodecane. The sampled gas was then sent through another chiller to further condense water vapor before introduction to the RLGA and Micro-GC instruments. Therefore, only dry concentrations with negligible amount of water or heavy fuel components can be measured and reported in this study. Heavier hydrocarbon components ($>C_5$) and water vapor were not quantified in this work, thus it was not possible to calculate wet concentrations due to the non-premixed nature of the reactor, as will be discussed later.

Flow visualization was conducted as part of the experimental investigation. Planar laser-induced fluorescence (PLIF) was used for instantaneous and non-intrusive diagnostics. The fuel consumption could be qualitatively inferred by selecting toluene as the tracer (5% by volume, consumed in catalytic reactions) [37, 38]. The excitation laser pulse by an Nd-YAG laser (maximum output 120 mJ/pulse, 266 nm) was expanded by light-sheet optics into a 10 mm high laser sheet. Toluene fluorescence then propagated through a BG280 band-pass filter (full width at half maximum 10 nm) and recorded by an intensified CCD camera. The toluene detection limit was estimated 600 ppm, assuming within the linear fluorescence regime and a signal-to-noise ratio of 3.0 [39].

To start the reactor when the platinum catalyst was used, the mesh was preheated by heated air (300 °C) until it emitted a red glow, indicating the initiation of catalytic reforming reactions. For the rhodium catalytic mesh, a higher air temperature (~400 °C) was initially applied and then reduced to 300°C because of higher required catalyst activation temperature. A gas phase flame was not observed during ignition and steady state operation condition. Upon catalyst light-off, thermal radiation from the mesh evaporated fuel from the liquid pool at a significantly higher rate than injecting hot air only. After the catalyst became active, it was found that the reaction could be sustained without requiring external air heating. However, the experiments reported here were conducted with an inlet air temperature of 300 °C to maintain the stability of the reactor over a larger range of airflow and various mesh location conditions.

Description of Experiments

Five different airflow and mesh location combinations were conducted for platinum and rhodium catalysts, respectively (Table 1). The total experimental durations for platinum and rhodium were approximately 200 hours and 120 hours, respectively. No catalyst degradation was observed during the experimental campaign as temperatures, sampled gas species concentrations were repeatable throughout. The mesh position indicates the distance of the mesh to the fuel pool (y value in Fig. 2(a)). The mesh location also affects the fuel vaporization rate through radiation heat transfer. Conditions 1-3 represent the efforts in changing mesh location with fixed airflow rate to study reforming performance at different molar carbon-to-oxygen ratio at the mesh location ($(C/O)_{mesh}$), a metric that was calculated by the developed 1-D model. Conditions 4 and 5 had mesh positions

in accordance with Conditions 2 and 3 but with a higher or lower airflow rate to vary $(C/O)_{mesh}$ and strain rate, defined as $(U_O+U_F)/L$, where U_O is the oxygen velocity, U_F is the fuel velocity and L is the distance between the outlets.

Table 1. Experimental conditions at different mesh locations and airflow rate.

Condition Number	Mesh Pos. (mm)	Platinum			Rhodium		
		Airflow (SLPM)	Fuel rate (mL/min)	$(C/O)_g$	Airflow (SLPM)	Fuel rate (mL/min)	$(C/O)_g$
1	3	7.2	2.8	2.35	7.2	3.9	3.27
2	4	7.2	2.4	2.01	7.2	3.5	2.93
3	5	7.2	2.3	1.93	7.2	3.2	2.68
4	3	10.9	3.6	1.99	14.0	5.2	2.24
5	5	6.2	2.3	2.26	6.0	3.4	3.46

The $(C/O)_g$ is the overall molar carbon-to-oxygen ratio calculated from the measured total airflow and the fuel evaporation measured from the side pool makeup flow. A syringe pump fed liquid fuel into the fuel pool to maintain the liquid level in the fuel pool; thus, the evaporation rate was equal to the fuel flow rate. It is worth noting that $(C/O)_g$ could not be directly controlled because the fuel evaporation rate was dependent on the amount of air injected into the reaction zone. The conditions listed in Table 1 were chosen to characterize the opposed-flow reformer under various conditions that cover a range of the interdependent $(C/O)_g$ and $(C/O)_{mesh}$ metrics.

One-Dimensional Reactor Model

An axisymmetric 1-D similarity model was developed to analyse the experimental reactor data and to infer the $(C/O)_{mesh}$ stoichiometry. Detailed chemical mechanisms for dodecane are not readily available in existing literature. Thus, a simplified, reduced model was developed to correlate axial catalytic mesh location with an estimated local carbon-to-oxygen ratio and to estimate the temperature distribution along the reactor centreline by solving a flame sheet model. The model

development is provided the Supplemental Information (SI). A series of assumptions were made in the model since the complete set of surface transport and chemistry parameters are not yet available for combination of fuel, catalysts, support, and thermodynamic conditions used in this study.

Axisymmetric similarity models are commonly used to analyse opposed-flow flame reactors. The classic flame sheet assumption for the opposed flame is often employed, which assumes that chemical kinetics at the reaction front are infinitely fast [30, 40]. In short, our model is similar to canonical opposed-flow flame reactor models but with some significant differences as depicted in Figure 3: 1) the mass flow of the fuel vapor is not directly controlled manually but rather determined by the heat transfer to the liquid fuel; 2) the reaction plane position is not at stoichiometric *C/O*, but can be adjusted with the mesh height and flow conditions (adjustable C/O_{mesh}); 3) the mesh radiates extra energy to the fuel pool compared with that of the opposed flame because of a higher radiative emissivity of the solid mesh; 4) The gas-phase reactions away from the mesh are negligible with a correspondingly lower temperature of such regions in the reactor. Mathematical details of the model can be found in the SI.

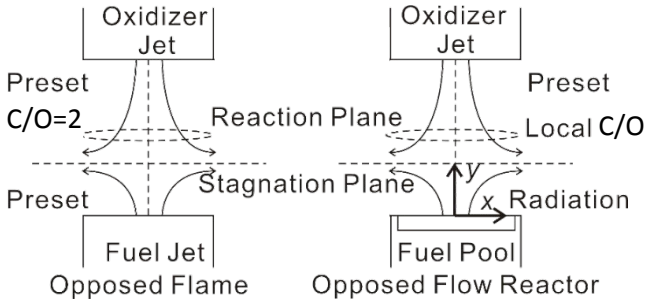

Figure 3. Schematic of the opposed-flow reactive volatilization model.

RESULTS AND DISCUSSION

Flow Visualization

Experimental conditions 1 and 4 with the platinum catalyst in Table 1 are used to demonstrate the flow

by PLIF, shown by straight dashed lines in Fig. 4 at the same location. Only one-half of the reactor domain is shown due to symmetry. Error due to light scattering at the edge of the catalytic mesh can be seen on the right-hand-side of the images. The radial fuel concentration (*x*-direction) below the catalytic mesh was nearly uniform for Condition 4. Fuel concentration decreased with axial distance (y-direction) due to fuel consumption and mass diffusion, while the fuel was completely depleted since no tracer was observed above the mesh. In contrast, toluene was present above the catalytic mesh (region circled by the dashed line in Fig. 4) in Condition 1, indicating incomplete fuel conversion on the mesh due to a lower airflow and a higher $(C/O)_{mesh}$. Additionally, fuel was not observed above the catalytic mesh in the other three conditions. These qualitative results show that the approximation of complete fuel conversion at the catalytic mesh made in the numerical modelling was reasonable for most of the experimental conditions.

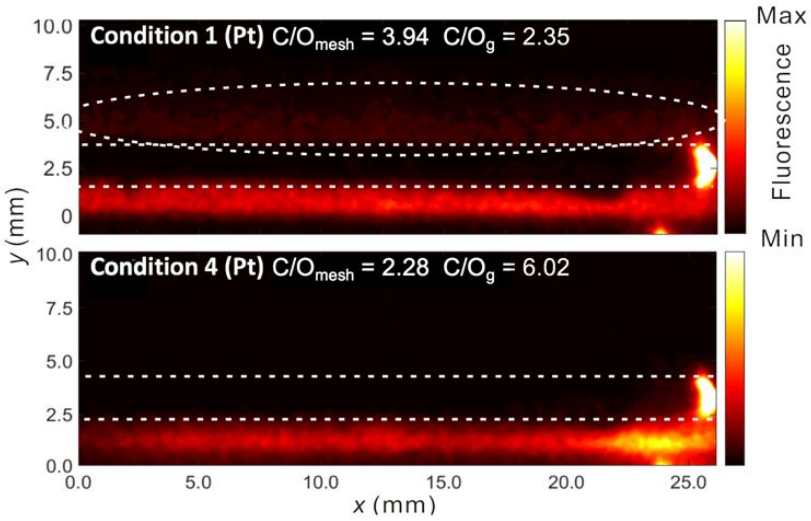

Figure 4. Laser visualization of the reaction by tracer (toluene) PLIF.

Temperature Profile

Condition 3 (Pt) is taken as an example to examine the 2-D temperature profile of the reaction zone through thermocouple mapping with resulting contour plot shown in Fig. 5. The mesh ring support blocked

0.75 mm space above and below the catalytic mesh resulted in a blank zone with no temperature measurement possible (represented by the blue-shaded zone in the figure). The highest axial temperature (~450 °C) was observed below the catalytic mesh and was about 50 °C higher than the corresponding position above the mesh. Temperature was highest at the centreline and decreased with radial distance due to convection and heat dissipation. Temperature near the fuel pool (~300 °C) was higher than the boiling temperature of n-dodecane (216 °C), providing the thermal driving force for fuel evaporation. Temperature mapping of other conditions with both catalytic materials was conducted. Trends and the temperature distributions were similar to the 2D contour plots shown in Fig. 5 and are therefore not shown for brevity.

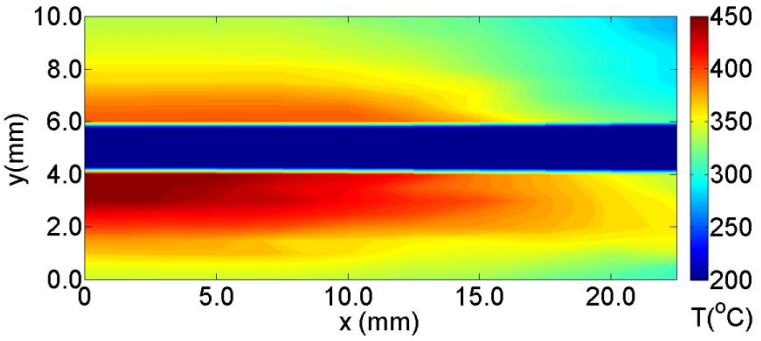

Figure 5. 2-D temperature contours measured by thermocouple mapping for Condition 3 with platinum catalyst. The blank region (1.5 mm distance) in the middle is due to catalytic mesh/ring support block.

One-dimensional temperature measurements along the reactor centreline for all conditions are further analysed and compared with model predictions as shown in Fig. 6. $(C/O)_{mesh}$ calculated by the developed 1-D similarity model is indicated in each subplot of the figure. For Conditions 1-3 with both catalysts, all parameters were kept the same except mesh location. As the mesh location moved closer to the pool, $(C/O)_{mesh}$ increased through the stoichiometric point mixture to a fuel-rich condition.

The modelled centreline temperature profiles were largely in agreement with experimental measurements. Predicted peak temperature in all these cases matched corresponding experiments with an error of less than 30 °C. The trend of temperature profile across conditions largely agreed with numerical modelling results. However, consistently higher measured temperatures on the air side of the mesh than predicted by the model suggest that gas-phase reactions could be occurring in that region. However, since the extent of gas-phase reactions is minor compared to those on the mesh, they likely had little effect on product distribution. Nevertheless, lacking the detailed mechanisms of n-dodecane CPOx, this model only provided a starting point for more detailed kinetic modelling.

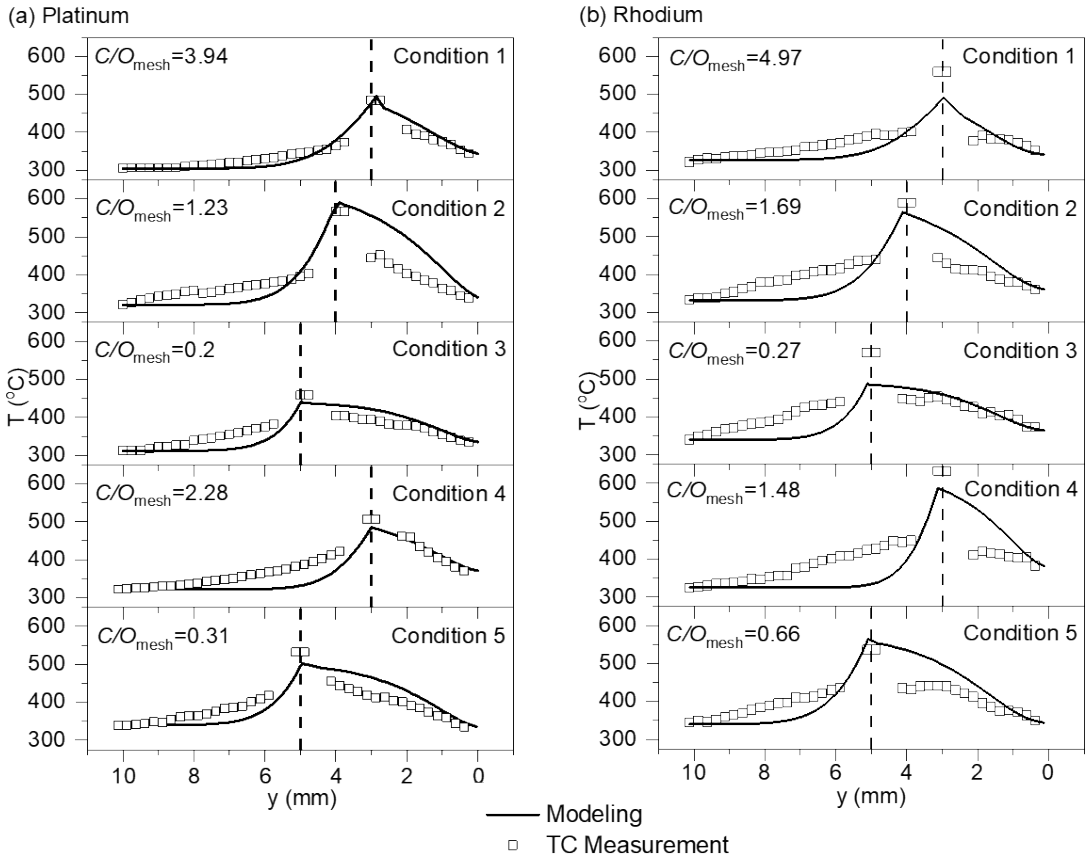

Figure 6. Comparison of 1-D temperature along the reactor centreline by experimental and model estimation for both catalysts. $(C/O)_{mesh}$ obtained from numerical modelling.

The range of $(C/O)_g$ in the experiments fell in the narrow range of 1.93 to 2.35 for platinum and from 2.24 to 3.46 for rhodium. Stable reactions on the mesh could be achieved over a range of $(C/O)_{mesh}$ (calculated) from 0.2 to3.94 for platinum and 0.27 to 4.97 for rhodium. This indicates that changing catalytic mesh position can be used to obtain desired local stoichiometry while maintaining a constant $(C/O)_g$. For example, a high $(C/O)_{mesh}$ (e.g. $(C/O)_{mesh}$ >3.25) may be used to increase the reforming efficiency defined by the ratio of product to reactant heating value at the expense of lower product hydrogen concentration. Mesh stoichiometry was also experimentally found to be extremely sensitive to axial mesh position, especially for rhodium; precise placement can be guided by modelling to optimize product distribution. A wide range of $(C/O)_{mesh}$ was achieved by changing the catalytic mesh location and airflow together while maintaining the reaction stable (Fig. 5, Conditions 4 and 5). Peak temperature increased as $(C/O)_{mesh}$ moved towards stoichiometric as expected. Quantitatively, the peak temperature increased by ~50 °C between Conditions 3 and 5 with the same mesh position.

Comparing platinum and rhodium catalysts results, it was found that the reactions with rhodium catalysts were less stable than those with the platinum catalyst. A maximum of 30 °C temperature variation was measured during rhodium testing compared to a variation of 10 °C for the platinum catalyst. The rhodium catalyst exhibited oscillatory behaviour, increasing the measured temperature variance [41-44]. Possible explanations for this phenomenon include the formation of surface oxide, its re-reduction on metal catalysts, and nonlinear dynamics. Strong low-frequency oscillations have been previously observed in natural gas oxidation over palladium catalysts attributed to surface palladium oxide formation, where the redox of palladium is similar to rhodium [30]. Also, the

measured rhodium reaction temperatures were higher than platinum at similar mesh locations and airflow conditions. This result likely stems from the higher activity of rhodium for converting fuel to partial oxidation products at the inlet air temperature and carbon-to-oxygen ratio ranges considered in the experiments. Further exploration of kinetics on the catalyst surface would be required to understand more detailed differences between the catalysts. Despite the simplicity of the flame sheet assumption, our model also confirmed experimental results showing that the temperature on either side of the catalytic mesh had low sensitivity to catalyst activity and selectivity.

Species profile

When interpreting the species results, it is important to note that an overall mass balance and C/O_g cannot be measured directly due to the open design of the reactor. From species measurement for Conditions 1 and 2 (Table 3), unburned n-dodecane, reformed heavy hydrocarbons, and water vapor were removed from the product samples prior to the RLGA analyser using a chilled water dropout. Therefore, all species concentrations presented here are on a dry basis. For a direct comparison with experiments (plotted in Fig. 6), unburned n-dodecane and water vapor components were removed from the flame sheet model results.

Table 2. Averaged species concentration (%) measured immediately above (i.e., the air side of) the catalytic mesh.

Condition	CH_4	C_2H_x	C_3H_x	C_4H_x	CO_2	CO	H_2
1 (Pt)	0.043	0.119	0.344	0.167	4.084	0.193	0.0
1 (Rh)	0.056	0.0	0.063	0.052	6.074	1.578	0.823
2 (Pt)	0.032	0.0	0.053	0.027	3.975	0.499	0.0
2 (Rh)	0.012	0.0	0.005	0.001	6.282	1.781	1.880

Comparing the two catalytic materials in Table 2 and Figure 7, selectivity towards syngas products was notably higher for rhodium than for platinum as expected from the literature [40]. Poor

hydrogen selectivity for the platinum catalyst indicates that short residence time reaction partial oxidization reforming (i.e., syngas production) did not occur. On the other hand, the platinum-coated meshes produced more light hydrocarbons than rhodium, indicating partial fuel conversion occurred without complete conversion to CO_2.

The difference in reforming product distribution between catalysts also explains the higher mesh temperature found for rhodium since the enthalpy of formation for syngas components are lower than light hydrocarbons. When comparing between the two conditions, more light hydrocarbons were produced in Condition 1 than Condition 2 for both catalysts, especially C2 – C4 species, on the oxidizer side (left region of mesh in Fig. 6). With $(C/O)_{mesh,1} > (C/O)_{mesh,2}$, confirmed by the modelling results, the assumption that changing mesh location alters $(C/O)_{mesh}$ is validated. Further, Condition 2 with rhodium catalyst produced more syngas than Condition 1 (H_2 and CO concentration increased from 1.578% to 1.781% and from 0.823% to 1.880%, respectively). Increased local $(C/O)_{mesh}$ in Condition 2 resulted in higher syngas production.

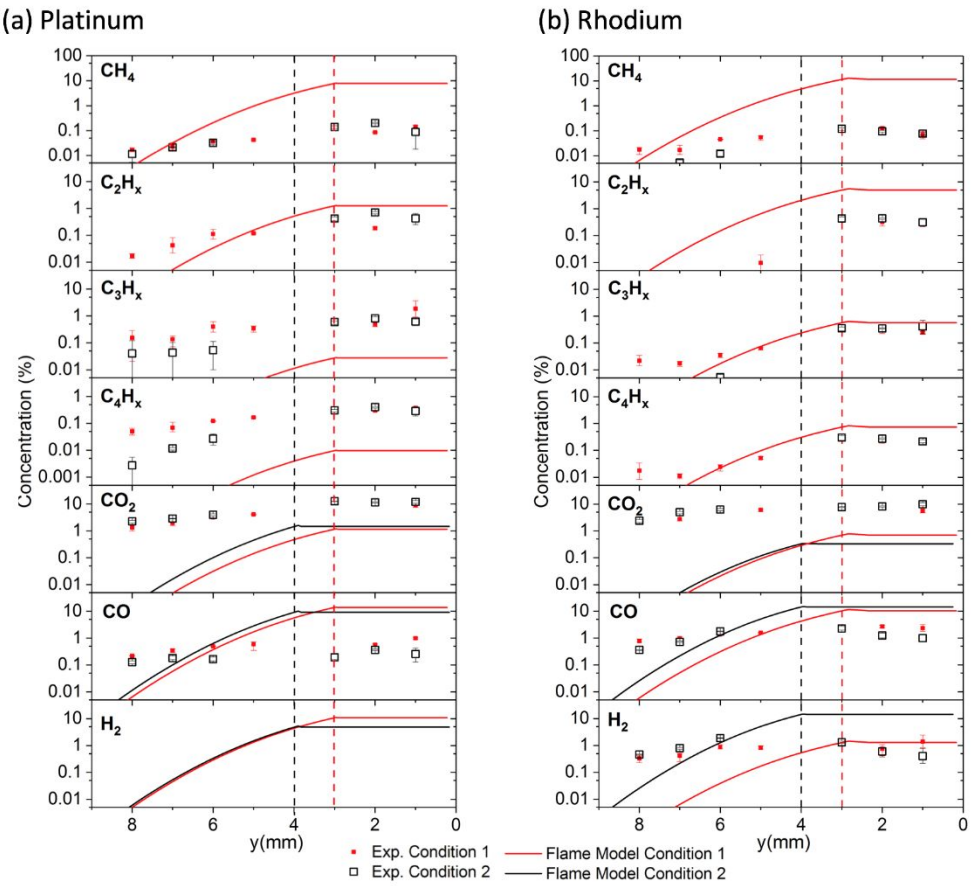

Figure 7. Experiment measurements and modelling results of species concentrations for Condition 1 and Condition 2 with both catalysts. Only dry components were considered.

Species concentration predictions by the flame sheet model are also plotted in Fig. 7. Overall, model predictions deviated from experiments. Specifically, the model prediction of light hydrocarbon concentrations was much lower, especially for Condition 2, where no light hydrocarbon production was predicted; rather, the flame sheet model predicted a significant amount of syngas components though the experiments suggested otherwise. For example, low CO concentration (<1%) was found experimentally and no hydrogen was produced with the platinum catalyst; however, the model predicted ~20 % hydrogen production for all cases. This result re-emphasizes the importance of using the correct surface chemistry for the catalytic mesh to predict accurate product distribution.

Although the simplified flame sheet model did not accurately predict species concentrations, it predicted relative spatial trends well. For example, a rapid decrease in product concentration with increasing axial distance (y) was observed above the catalytic mesh for both experiment and model. The model also agreed with experiments showing that dry species concentration on the fuel side of the catalytic mesh (right size) held a constant value. Measured species concentration did not vary significantly when moving the probe away from the catalytic mesh for either condition. Meanwhile on the oxidizer side, species concentrations dropped rapidly when moving the probe away from the catalytic mesh, which can be explained using the model (see SI for model details). The predicted species diffusion was less significant than in experimental measurements, indicating that the model requires incorporation of different diffusivities for various species.

Based on the results discussed here, the 1-D simulation approach appears capable of modelling the physics of the opposed-flow catalytic reactor due to its reasonable accuracy in predicting temperature profile and the ability to predict species trends. However, the model requires more accurate catalyst chemistry and transport properties to be known, especially at the catalytic mesh surface to predict species concentration. The 1-D flame sheet model can also be used as the initial solution for a 1-D model with detailed chemistry, which will be developed in future work.

Surface Carbon Deposition Potential

Catalyst deactivation by surface carbon deposition in CPOx reactors is primarily controlled by the fuel-air mixture and catalyst temperature. A C-H-O ternary diagram is frequently used to understand carbon deposition regimes for different hydrocarbons [45, 46]. Figure 8 shows the carbon deposition region for

different isotherms[21]. Pertinent to this study, n-dodecane CPOx is noted as the red line in the C-H-O ternary diagram. Experimental conditions are indicated as circles for rhodium and rectangles for the platinum catalyst. Based on the opposed-flow configuration and surface temperature (500-600 ˚C) of the tested catalyst, carbon deposition is favoured at $(C/O)_{mesh}$ >3.25. The experimental results agreed with this as there was no carbon deposition observed. As discussed in previous sections, the $(C/O)_{mesh}$ determines species production in the opposed-flow reactor, unlike in premixed reactors, where only $(C/O)_g$ is of importance. For example, Condition 5 with rhodium catalyst was fuel-rich globally but was lean at the mesh surface (C/O_g=3.45, C/O_{mesh}=0.66), leading to lean combustion products being formed, not shown in Figure 7 for brevity.

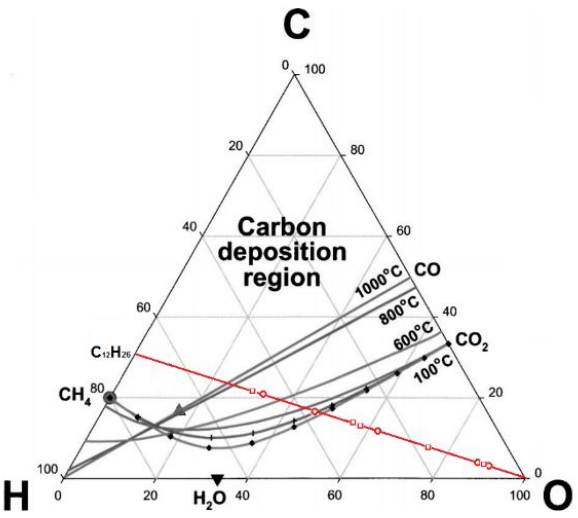

Figure 8. C-H-O ternary diagram of n-dodecane carbon deposition (adapted from[21]).

No observable carbon deposition occurred for Condition 1 (C/O_{mesh}=3.94 and 4.97, respectively) with platinum or rhodium catalyst over the experimental duration as would be expected from the ternary diagram. One possible explanation for this result is inadequate time for soot formation [47, 48] due to the low residence duration of the gas over the catalyst substrate. A major precursor species of soot formation, C_2H_2 requires

at least 100 ms of residence time in conventional reforming reactors, substantially more than the residence times over the catalytic mesh (approximately 16.89 ms for Condition 1)[49-51].

Short contact time in opposed-flow reactors could be a way to limit carbon deposition while still performing POx reforming at high $(C/O)_{mesh}$ unobtainable in premixed reactors. Fuel-rich POx may be desirable in applications where complete conversion to syngas is not needed, like in engine applications where partially reacted hydrocarbons can alter fuel combustion regimes to enable high efficiency or low pollutant emissions formation[9]. Additionally, adjustable mesh position in the opposed-flow reactor allows a rapid change of $(C/O)_{mesh}$, which could enable quick catalyst regeneration should carbon be formed on the surface.

Conclusions

This research explored a non-premixed opposed-flow reactive volatilization reactor for reforming and evaporating low volatility fuels. The CPOx reactor design was adapted from classical opposed-flow flame reactors by incorporating a catalytic mesh between the air inlet and liquid fuel pool. It was demonstrated by experiments with n-dodecane where 2-D temperature data were collected, and a toluene fluorescence technique was used to identify fuel distribution. A modified 1-D model was used, assuming that the catalytic mesh acts as a flame sheet, converting all of the fuel to equilibrium products. $(C/O)_{mesh}$ is shown to be very sensitive to axial catalyst location, altering reforming efficiency and product distribution. The flame sheet model may be useful as a starting approximation for more detailed chemical modelling or for predicting mesh location to optimize reformed product species while detailed surface chemical mechanisms were needed.

More broadly, the non-premixed reactive volatilization reactor developed in this research includes the benefit of available and adjustable $(C/O)_{mesh}$ to allow selectivity to CPOx products not practically allowed by premixed reactors by adjusting the catalyst position without altering the global carbon-to-oxygen ratio. By virtue of its short residence time and avoidance of premixed gas phase reactions, the opposed-flow reactor has potential to lower operation temperature and thus avoid catalyst deactivation. The design has merit for evaporating and partially reacting liquid hydrocarbons at high $(C/O)_g$, a regime where traditional premixed reformers cannot operate due to catalyst deactivation due to carbon deposition.

From an application perspective, the axi-symmetric opposed-flow reactor presented here is not well suited to direct scale-up since it cannot obtain full fuel conversion. The open nature of the axi-symmetric opposed-flow configuration inevitably leads to unreacted fuel and oxidizer as it does in the related canonical opposed flow flame reactor. However, configurations could be imagined, including annular concepts[27], that retain the advantages of the opposed-flow reactor while potentially resulting in complete fuel conversion. Despite this disadvantage of the axisymmetric design reported here, the presented research establishes the concept of simultaneous vaporization and reforming of liquid fuels, investigating fundamental concepts such as initial chemistry of reforming reactions, and offers insights on designing structurally more complex industrial non-premixed reformers. These unique characteristics motivate the potential benefits of further work to study derivative non-premixed configurations. Future work with this novel opposed-flow design includes incorporating simple fuels such as methane and laser diagnostics for temperature and intermediate speciation characterization.

CONFLICTS OF INTEREST

The authors declare no conflicts of interest.

ACKNOWLEDGEMENTS

The authors would like to thank Joseph Viavattine and Dereck Dasrath at University of Minnesota for their contribution in designing, fabricating, and testing the reactor used in this research. This work was supported by the U.S. National Science Foundation [grant number 1350709].

References

1. K. Aasberg-Petersen, J.-H. B. Hansen, T. Christensen, I. Dybkjaer, P. S. Christensen, C. S. Nielsen, S. W. Madsen and J. Rostrup-Nielsen, *Applied Catalysis A: General*, 2001, **221**, 379-387.
2. J. N. Armor, *Applied Catalysis A: General*, 1999, **176**, 159-176.
3. M. V. Twigg, 1996.
4. S. Sengodan, R. Lan, J. Humphreys, D. Du, W. Xu, H. Wang and S. Tao, *Renewable and Sustainable Energy Reviews*, 2018, **82**, 761-780.
5. R. C. Samsun, D. Krekel, J. Pasel, M. Prawitz, R. Peters and D. Stolten, *J Power Sources*, 2017, **355**, 44-52.
6. X. L. Ma, L. Sun and C. S. Song, *Catal Today*, 2002, **77**, 107-116.
7. D. Fennell, J. M. Herreros, A. Tsolakis, H. Xu, K. Cockle and P. Millington, *GDI engine performance and emissions with reformed exhaust gas recirculation (REGR)*, Report 0148-7191, SAE Technical Paper, 2013.
8. S. R. Gomes, N. Bion, G. Blanchard, S. Rousseau, V. Bellière-Baca, V. Harlé, D. Duprez and F. Epron, *Applied Catalysis B: Environmental*, 2011, **102**, 44-53.
9. J. Hwang, X. Li and W. Northrop, *Exploration of Dual Fuel Diesel Engine Operation with On-Board Fuel Reforming*, Report 0148-7191, SAE Technical Paper, 2017.
10. I. Kang, J. Bae and G. Bae, *J Power Sources*, 2006, **163**, 538-546.
11. C. Song and W. Pan, *Catal Today*, 2004, **98**, 463-484.
12. C. Karakaya, L. Maier and O. Deutschmann, *International Journal of Chemical Kinetics*, 2016, **48**, 144-160.
13. C. Karakaya, H. Karadeniz, L. Maier and O. Deutschmann, *ChemCatChem*, 2017, **9**, 685-695.
14. J. J. Krummenacher, K. N. West and L. D. Schmidt, *Journal of Catalysis*, 2003, **215**, 332-343.
15. T. Kaltschmitt, L. Maier, M. Hartmann, C. Hauck and O. Deutschmann, *Proceedings of the Combustion Institute*, 2011, **33**, 3177-3183.
16. J. A. Moulijn, A. Van Diepen and F. Kapteijn, *Applied Catalysis A: General*, 2001, **212**, 3-16.
17. R. M. Heck, S. Gulati and R. J. Farrauto, *Chemical Engineering Journal*, 2001, **82**, 149-156.

18. H. Zhong, X. Mao, A. C. Rousso, C. L. Patrick, C. Yan, W. Xu, Q. Chen, G. Wysocki and Y. Ju, *Proceedings of the Combustion Institute*, 2020.
19. J. Krummenacher, *Journal of Catalysis*, 2003, **215**, 332-343.
20. J. R. Salge, B. J. Dreyer, P. J. Dauenhauer and L. D. Schmidt, *Science*, 2006, **314**, 801-804.
21. J. L. Colby, P. J. Dauenhauer and L. D. Schmidt, *Green Chemistry*, 2008, **10**, 773-783.
22. J. J. Krummenacher and L. D. Schmidt, *Journal of Catalysis*, 2004, **222**, 429-438.
23. H. Tsuji, *Progress in energy and combustion science*, 1982, **8**, 93-119.
24. T. Aicher and L. Griesser, *J Power Sources*, 2007, **165**, 210-216.
25. M. Iamarino, P. Ammendola, R. Chirone, R. Pirone, G. Ruoppolo and G. Russo, *Industrial & engineering chemistry research*, 2006, **45**, 1009-1013.
26. J. Hong, P. Kirchen and A. F. Ghoniem, *Journal of membrane science*, 2012, **407**, 71-85.
27. K. Seshadri, S. Humer and R. Seiser, *Combustion Theory and Modelling*, 2008, **12**, 831-855.
28. W. Liu, D. Zhu, N. Wu and C. K. Law, *Combustion and Flame*, 2010, **157**, 259-266.
29. A. Ehn, J. Zhu, X. Li and J. Kiefer, *Applied spectroscopy*, 2017, **71**, 341-366.
30. R. J. Kee, M. E. Coltrin and P. Glarborg, *Chemically reacting flow: theory and practice*, John Wiley & Sons, 2005.
31. R. J. Kee, W. Yang, L. L. Raja and C. A. Wolden, *Proceedings of the Combustion Institute*, 2000, **28**, 1381-1388.
32. U. Niemann, K. Seshadri and F. A. Williams, *Combustion and Flame*, 2015, **162**, 1540-1549.
33. R. K. A. Kailasanathan, T. L. B. Yelverton, T. Fang and W. L. Roberts, *Combustion and Flame*, 2013, **160**, 656-670.
34. C. R. Shaddix, *Correcting thermocouple measurements for radiation loss: a critical review*, Sandia National Labs., Livermore, CA (US), 1999.
35. K.-F. V. Wong, 2003.
36. R. M. Fristrom and A. A. Westenberg, *Flame structure*, McGraw-Hill, 1965.
37. J. Sjöholm, J. Rosell, B. Li, M. Richter, Z. Li, X.-S. Bai and M. Aldén, *Proceedings of the Combustion Institute*, 2013, **34**, 1475-1482.
38. S. Kaiser, M. Schild and C. Schulz, *Proceedings of the combustion institute*, 2013, **34**, 2911-2919.
39. S. C. Eichmann, J. Trost, T. Seeger, L. Zigan and A. Leipertz, *Optics express*, 2011, **19**, 11052-11058.
40. D. Keyes and M. Smooke, *Journal of Computational Physics*, 1987, **73**, 267-288.
41. R. Imbihl and G. Ertl, *Chemical Reviews*, 1995, **95**, 697-733.
42. P. J. Berlowitz, C. H. Peden and D. W. Goodman, *The Journal of Physical Chemistry*, 1988, **92**, 5213-5221.
43. J. Singh, M. Nachtegaal, E. M. Alayon, J. Stötzel and J. A. van Bokhoven, *ChemCatChem*, 2010, **2**, 653-657.
44. Y. H. Hu and E. Ruckenstein, *Industrial & engineering chemistry research*, 1998, **37**, 2333-2335.
45. K. Sasaki and Y. Teraoka, *Journal of The Electrochemical Society*, 2003, **150**, A885-A888.
46. C. H. Wendel, P. Kazempoor and R. J. Braun, *J Power Sources*, 2016, **301**, 93-104.
47. K. Dewa, K. Ono, A. Watanabe, K. Takahashi, Y. Matsukawa, Y. Saito, Y. Matsushita, H. Aoki, K. Era and T. Aoki, *Combustion and Flame*, 2016, **163**, 115-121.
48. K. Ono, M. Yanaka, S. Tanaka, Y. Saito, H. Aoki, O. Fukuda, T. Aoki and T. Yamaguchi, *Chemical engineering journal*, 2012, **200**, 541-548.
49. M. Hartmann, T. Kaltschmitt and O. Deutschmann, *Catal Today*, 2009, **147**, S204-S209.
50. M. R. Gray and W. C. McCaffrey, *Energy & fuels*, 2002, **16**, 756-766.

51. M. Ruiz, A. Callejas, A. Millera, M. Alzueta and R. Bilbao, *Journal of analytical and applied pyrolysis*, 2007, **79**, 244-251.